computer aided technologies for additive manufacturing

HORIZON 2020

VALIDATION STRATEGY FOR THERMAL ANALYSIS OF MD PROCESS

Deliverable D4.3

Circulation:	PU: Public
Lead partner:	Centre Internacional de Mètodes Numèrics en Enginyeria (CIMNE)
Contributing partners:	
Authors:	Michele Chiumenti, Eric Neiva, Joan Moya
Quality Controllers:	Bjørn Ellingsen, Rafael Vázquez
Version:	1.0
Date:	24.12.2016

Consisting of

SINTEF	STIFTELSEN SINTEF, Department of Applied Mathematics, Oslo, Norway
Fraunhofer	Fraunhofer IGD, Interaktive Engineering Technologien, Darmstadt, Germany
DFKI	Deutsches Forschungszentrum für Künstliche Intelligenz GmbH DFKI Innovative Factory Systems, Kaiserlautern, Germany
CNR-IMATI	Consiglio Nazionale Delle Ricerche Instituto di Matematica Applicata e Tecnologie Informatiche, Genova & Pavia, Italy
CIMNE	Centre Internacional de Metodes Numerics en Enginyeria Civil Engineering, Barcelona, Spain
ARCTUR	ARCTUR Racunalniski Inzeniring Doo, R&D, Nova Gorica, Slovenia
BOC	BOC ASSET Management GmbH, Innovation Group, Wien, Austria
Missler	Missler Software Missler Software Service Department, Ramonville St Agne, France
Jotne	Jotne EPM Technology AS, Aeronautics, Space and Defense, Oslo, Norway
STAM SRL	STAM SRL, R&D Department, Genova, Italy
TRIMEK SA	TRIMEK SA, R&D, Altube-Zuia (Alava), Spain
Tronrud	Tronrud Engineering AS, 3D Printing, Hønefoss, Norway
NOVATRA	NOVATRA, Varennes Saint Sauveur, France

Document History

Version[1]	Issue Date	Stage	Content and Changes
0.8	29.11.2016	Complete	Ready for internal revision
0.9	21.12.2016	Complete	Ready for quality control
1.0	24.12.2016	Complete	Ready to be submitted to Project Officer

[1] Integers correspond to submitted versions

EXECUTIVE SUMMARY

The purpose of this document is to describe the validation strategy and calibration results for the **thermal finite-element framework of the metal deposition process** occurring during the build of an object by Additive Manufacturing. This finite-element framework has already been detailed in *Deliverable 4.2: Thermal analysis framework for MD process*.

The document is structured as follows: Section 1 provides some context of the tasks of Work Package 4 and a brief description of the two main families of powder-based metal Additive Manufacturing technologies –powder-bed and blown-powder–, a comparison of the two technologies both from the physical and numerical viewpoints follows, and an overview of the different numerical simulation approaches closes the section; Section 2 addresses the experimental calibration of the model for powder-bed technologies with experimental data obtained from the *Monash Centre for Additive Manufacturing* (MCAM) in Melbourne, Australia; Section 3 presents the results of an experimental campaign carried out at the *State Key Laboratory of Solidification Processing* (SKLSP) in Xi'an, China, to calibrate the model for blown-powder technologies; finally, Section 4 sums up the main conclusions of the work and some informative annexes and lists complete this document.

TABLE OF CONTENTS

LIST OF FIGURES

LIST OF TABLES

LIST OF ABBREVIATIONS

AM	Additive Manufacturing
CAD	Computer-Aided Design
CAx	Computer-Aided Technologies
CAxMan	Computer-Aided Technologies for Additive Manufacturing
COMET	COupled MEchanical and Thermal
CLI	Common Layer Interface file format
FE	Finite Element
FEM	Finite-Element Method
FEA	Finite-Element Analysis
HAV	Heat Affected Volume
HPC	High-Performance Computing
HTC	Heat Transfer Coefficient
MCAM	Monash Centre for Additive Manufacturing
MD	Metal Deposition
SKLSP	State Key Laboratory of Solidification Processing

1 INTRODUCTION

1.1 OVERVIEW OF WORK PACKAGE 4

Work Package (WP) 4 *Thermal and stress analysis* aims to develop a numerical simulation tool of the metal deposition process by additive manufacturing with powder methods, with the purpose of analysing the temperature evolution and the subsequent stress field generated by the thermal exchanges, finally estimating the residual distortions induced in the manufactured metal part.

The final objective of the whole Work Package is to develop a useful simulation tool enabling the optimization of a product design, allowing a minimization of structural issues deriving from these stresses and allowing the design of efficient supporting structures in the part.

The intended simulation tool will be based on a modular software framework, whose structure is shown in FIGURE 1.

FIGURE 1 – SOFTWARE MODULES DEVELOPED IN WP4

FIGURE 1 underlines the three-step procedure for the simulation of the AM process developed in Work Package 4. This comprises:

- The pre-processing module is a graphical interface able to collect all the necessary information to run the numerical simulation. Here the user can specify the process parameters as well as the material data to feed the constitutive models characterizing the material behaviour. The parameters needed are:
  - Domain: This can be the CAD geometry representing the part and the corresponding support structures, or just the open space where the AM process will take place;
  - Finite Element (FE) mesh: a Finite Element (FE) discretization of the domain;
  - Process parameters for the AM process: including the scanning sequence, the size of the welding pool and the thickness of the deposited/sintered layer
  - Boundary conditions for thermal and mechanical analysis;
  - Material data: that characterizes the behaviour of the chosen material in the entire temperature range;
- The solver module, the software kernel performing the calculations of the numerical simulation of the process, according to the input specifications collected in the pre-processing phase;
- The post-processing module, where it is possible to show the results obtained from the simulation.

1.2 METAL DEPOSITION PROCESSES BY AM WITH POWDER METHODS

Although the first polymer-based commercial systems for 3D printing were introduced before the 1990s, it was not until 1998 when Electro Optical Systems (EOS) commercialised the first direct metal Additive Manufacturing (AM) system.

Most direct metal systems work using a point-wise method and nearly all of them utilize metal powders as input. Nowadays, there are two different families of AM processes using metal *powder* technology under rapid development:

1. *Powder-bed technologies*: Creates objects by focussing the heat source to melt regions of a powder bed according to the user-defined scanning sequence. Common technologies that rely on this principle are **Direct Metal Laser Sintering (DMLS)**, Electron Beam Melting (EBM), Selective Heat Sintering (SHS), Selective Laser Melting (SLM) and Selective Laser Sintering (SLS).

   The *Use Cases* for the CAxMan project will be produced with the EOSINT-M280. This machine uses the DMLS technology. Therefore, **DMLS** is the **target technology** for the thermal and stress analysis.

2. *Blown-powder technologies*: Builds parts by focussing the thermal energy on the substrate to form a melting pool where the powder is blown. The following coalescence process generates a new layer of material above the original substrate. Laser Engineered Net Shaping (LENS) and Laser Solid Forming (LSF) belong to this technology.

The numerical simulation of the thermo-mechanical analysis requires the understanding of these manufacturing technologies. Let us briefly review powder-bed and blown-powder technologies:

A typical printing process with powder-bed technologies, such as DMLS, occurs in a closed chamber with a gas[2] controlled atmosphere and consists of the following steps (see FIGURE 2):

1. A powder layer of typically 30-60 microns is spread over the building platform
2. A laser melt the region of powder that belongs to the first cross section
3. The building platform is lowered to accommodate a new layer
4. A new layer of powder is spread over the previous layer with the levelling blade
5. Steps 2. to 4. are repeated until the whole model is created
6. Loose unfused powder is removed during post processing

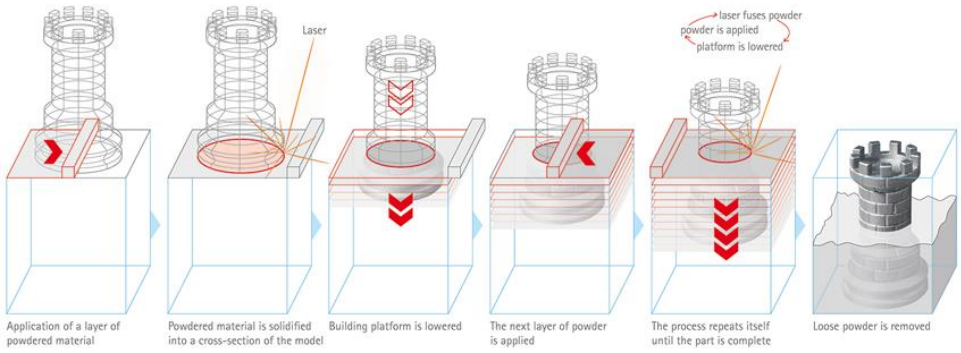

FIGURE 2 - SCHEMATIC REPRESENTATION OF AM PROCESS BY POWDER-BED (SOURCE: EOS.COM)

[2] According to EOS recommendations, Argon is used when printing with Titanium, Aluminium and Inconel. For maraging steel (MS1), Nitrogen is used.

In the case of blown-powder technologies, metal powder is blown coaxially to a laser beam. The laser melts the powder into the melt pool generated on the surface of the substrate and both form a metallurgical bond when cooled. As shown in FIGURE 3, a substrate is first clamped in a closed chamber with an argon-controlled atmosphere. Then, a laser melts the substrate while blowing the powder in it. The typical size of the new layer is 300 microns.

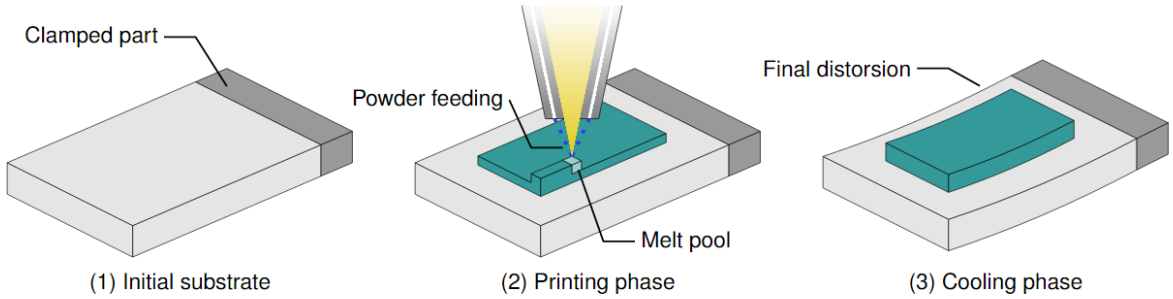

FIGURE 3 – SCHEMATIC REPRESENTATION OF AM PROCESS BY BLOWN-POWDER

1.2.1 Powder-bed vs blown-powder methods

As seen in *Deliverable 4.2 Thermal analysis framework for MD process*, the same thermal model is able to deal with both families of metal-powder AM manufacturing processes. However, they are characterized by different process parameters and different mechanisms of heat dissipation (boundary conditions). This leads to different thermal responses. In this section, all these technology-specific aspects are reviewed.

1.2.1.1 Technology-specific process parameters

Layer thickness: It is typically of 30 – 60 [μm] for powder-bed, while ≈ 300 [μm] for blown-powder technologies. This means the same part printed with powder-bed methods needs around 5 – 10 times more layers than with blown-powder methods.

Therefore, assuming a high-fidelity strategy (reproducing exactly the same scanning sequence as the actual process), the numerical simulation of the powder-bed technology requires around 5-10 more time steps than for blown-powder. Simplified methods, where a layer-by-layer or even multi-layer-by-multi-layer sequence is assumed can drastically reduce the computational cost of the simulation.

Laser power and focus: The laser power in powder-bed machines ranges between 100 – 400 [watt] focussed on through the powder-bed thickness to sinter the new layer. Alternatively, for blown-powder the laser source is of about 2000 [watt] and focussed on the substrate (or the previously deposited layer) to form the melt pool.

Build times: In powder-bed processes, the scanning speed is around 10 times faster than for blown-powder technology. Observe that to build the same piece, the metal deposition rate is of the same order for both technologies, because of the difference in the layer thickness.

Relocation: this is the delay time when the laser beam is paused. For powder-bed technologies it is mainly the time necessary to spread a new powder-bed. For the EOSINT-M280 machine, it takes about 1.5 seconds to lower the platform and 7.5 seconds to recoat a new layer. For blown-powder technologies, the delay time is mainly due to the re-positioning of the laser. The laser moves from the end point of one hatch to the starting point of the next hatch. The backward speed is about 5 to 10 times faster than the scanning speed.

	Powder-bed	*Blown-powder*
Layer thickness	1	10
Scanning speed	1	1/10
Laser power	1	10
Deposition rate	1	1

TABLE 1 - COMPARED ORDERS OF MAGNITUDE
OF MAIN PRINTING PARAMETERS FOR METAL-POWDER AM

This given, the powder-bed technology is a very local process in the sense that the Heat Affected Zone (HAZ) results to be much smaller than in blown-powder processes. Hence, both the temperature gradients and the stress distribution are mostly localized at the HAZ and do not depend on the rest of the component. This is the main argument of the simplified methods such as the shrinkage method [1]. Those methods require much less computational cost while retaining the main structural behaviour of high-fidelity analysis, as discussed in Section 1.2.2

Supporting structures: in powder-bed methods, if any external or internal surface of the part has an angle greater than 45º with respect to the vertical plane, the underlying powder is not able to withstand the weight of the piece. This leads eventually to excessive part distortion. To deal with these kinds of overhangs, it is necessary to add supporting structures that are printed together with the part. This practice is exclusive of powder-bed technologies. The supporting structures are lighter features to support the part during the printing phase and designed to be easily removed at a post-process phase. They are generally located between the base plate and the lower surface of the part or among internal surfaces (e.g. to generate holes) as shown in FIGURE 3.

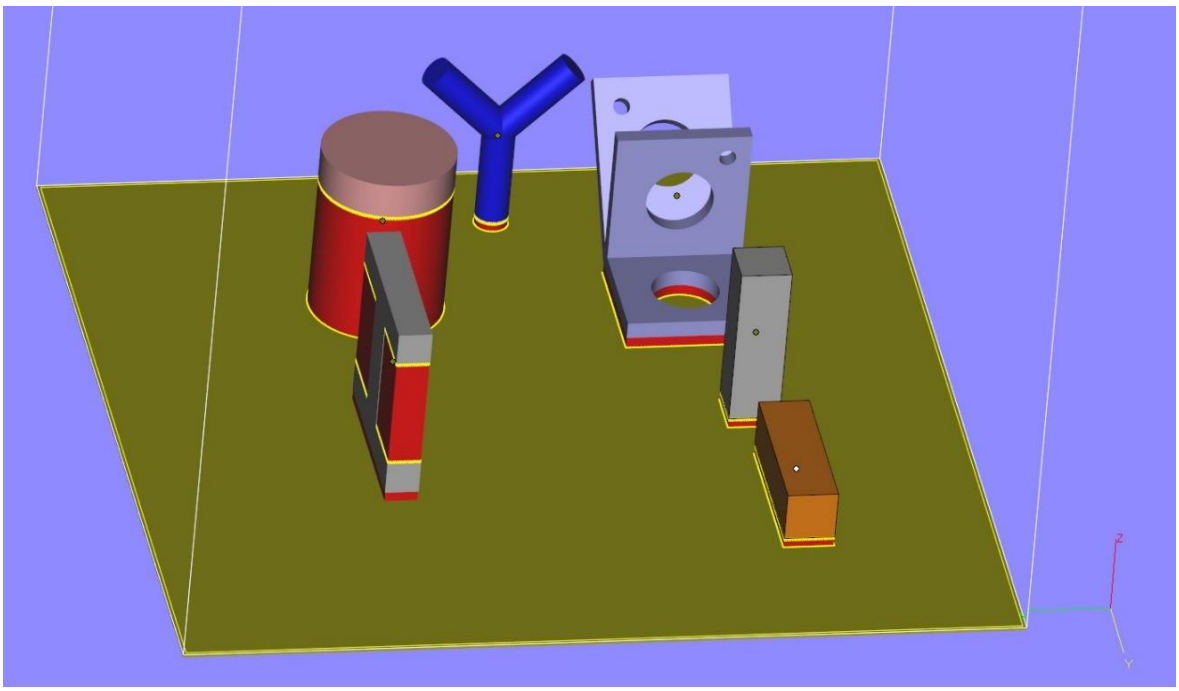

FIGURE 4 – SEVERAL SAMPLES GENERATED FOR PRINTING. RED REGIONS INDICATE
SUPPORTING STRUCTURES (SOURCE: TRONRUD, CAXMAN EROOM).

The location of supporting structures is basically designed thanks to the expertise of the machine operator and by using numerical tools checking the orientation of the external surfaces of the part to be printed. Hence, an appropriate definition of the supporting structure is crucial to guarantee the process feasibility.

On the one hand, if the supporting structure is too light, it can break during the printing process, because it is not able to withstand the thermal stresses of the piece. When this happens, the stresses accumulated are released producing part distortions that can block the levelling blade during the powder spreading of the following layer.

On the other hand, if the supporting structures are too rigid, the thermal stresses may crack the part.

Finally, it can be difficult, expensive and time-consuming to remove all the supporting structures after the printing process, so their location must be accurately designed.

1.2.1.2 Heat loss mechanisms and thermal boundary conditions

In both technologies the printing process is performed in a closed chamber with a controlled gas atmosphere to prevent oxidation. Both technologies can adopt laser or EB energy sources. The main difference is the heat dissipation mechanism.

For powder-bed technologies, the part is built above the building platform. Hence, the main mechanism of heat dissipation is by heat conduction through the building platform. The lateral surfaces of the part are in contact with the surrounding spread powder (not sintered). The heat loss is by conduction through a porous media which generally shows very low heat conductivity. Finally, the top surface of the part is in contact with the argon atmosphere, till it is covered by the new powder layer. During the sintering process, this surface cools down very fast by heat convection and heat radiation mechanisms.

Observe that, the density of the metal powder bed can be obtained by weighting the powder bed. More complex is the determination of the conductivity of metal powders. This is frequently estimated by using empirical expressions in terms of the conductivity of the bulk material and the conductivity of the surrounding gas as a function of the actual porosity of the powder bed.

Alternatively, it can be noted that typically the volume of the unsintered powder is much higher than the one of the actual component. For the sake of simplicity, the unsintered powder bed could not be considered in the model to reduce the computational time of the simulation. In this case, heat conduction through the powder-bed is replaced by an equivalent heat loss by convection to be calibrated through sensitivity analysis.

On the other hand, for blown-powder technologies, all external surfaces of the part are exposed to the controlled argon atmosphere within the closed chamber of the machine. Thus, heat convection and heat radiation are the main mechanisms of heat loss. At the clamped surfaces of the substrate, heat is lost by conduction through the clamping system.

1.2.2 Numerical simulation strategies

Concerning the thermal and stress simulation analysis of the AM process, three possible approaches can be identified:

- The *coupled thermo-mechanical simulation* is the most time-consuming option but it provides the most accurate results. The full size simulation may be run only on parallel HPC infrastructure. A simplified approach can consist of assuming a simplified scanning sequence by simulating several (e.g. 10) layers at the same time, not taking into account the specific scanning sequence, thus reducing the number of steps.

- A *pure thermal analysis* able to compute the temperature evolution during the building process induced by the scanning strategy. The objective is to find out the optimal scanning sequence to minimize the thermal field induced by the sintering process. High temperatures and temperature gradients generate strong thermal deformations and, consequently, higher plastic strains that transform into large distortions.

- A *pure mechanical simulation* can be used to study the residual stresses in the manufactured part by assuming either predefined thermal strains (shrinkage method) or plastic deformations (inherent strains method). As explained in Section 1.2.1.1 powder-bed processes can be regarded as more local than blown-powder, because the effect of the HAZ has a lower influence in the global temperature distribution of the part, that is, the process is globally more isothermal. As a consequence, the solution of the global problem is less important to compute the local thermal shrinkage induced by the heat source during the sintering process. This is the basis of the shrinkage volume method [1] and it is currently being implemented within Task 4.3 of WP4, as an efficient alternative to predict the residual stresses using powder-bed methods, the reference metal AM technology in the CAxMan project. This simplified approach results in less accurate results than the fully coupled FE framework, but is an efficient and reliable technique to make predictions within the industrial time frames.

2 MODEL CALIBRATION FOR POWDER-BED METHODS

2.1 EXPERIMENTAL SETTING

An experimental campaign was carried out at the *Monash Centre for Additive Manufacturing* (MCAM) in Melbourne, Australia, with the purpose of calibrating for powder-bed methods the thermal analysis FE framework described in *Deliverable 4.2: Thermal analysis framework for MD process*.

The printing system employed for the experiments is the EOSINT M280 from Electro Optical Systems (EOS) GmbH. This is the same printer that is available to produce the Use Cases of the CAxMan project. It makes use of an Yb-fibre laser with variable beam width and power up to 400 [W].

The printing process is carried out in a closed 250x250x325 [mm] chamber in a controlled argon atmosphere to prevent oxidation of the part. The argon flow is kept laminar.

In FIGURE 6 is shown the samples geometry for the experimental validation. These consist of two specimens printed simultaneously: a thin wall measuring 5x80x50 [mm] and a thicker wall measuring 40x80x50 [mm]. The two walls are separated by a distance of 40 [mm].

The building platform has dimensions of 252x252x45 [mm]. Ti64 powder has been used for the printing operation.

The thermocouples for the temperature measurements have been welded at different locations of the 2 specimens. For this reason, the printing job had to be interrupted after an initial deposition of 20.24 [mm] high and the powder bed had to be removed. Four thermocouples have been installed in each sample: the first three separated by 5 [mm] in the vertical direction and the fourth one displaced 10 [mm] horizontally from the top one, as shown in FIGURE 5. Next, the powder bed has been restored, and scanning sequence resumed, as described in FIGURE 7.

K-type thermocouples and a Graphtec GL-900 8 high-speed data-logger were used for the data gathering. Temperature data could be measured only from six channels, because the fourth channel in both walls was broken during setup operations.

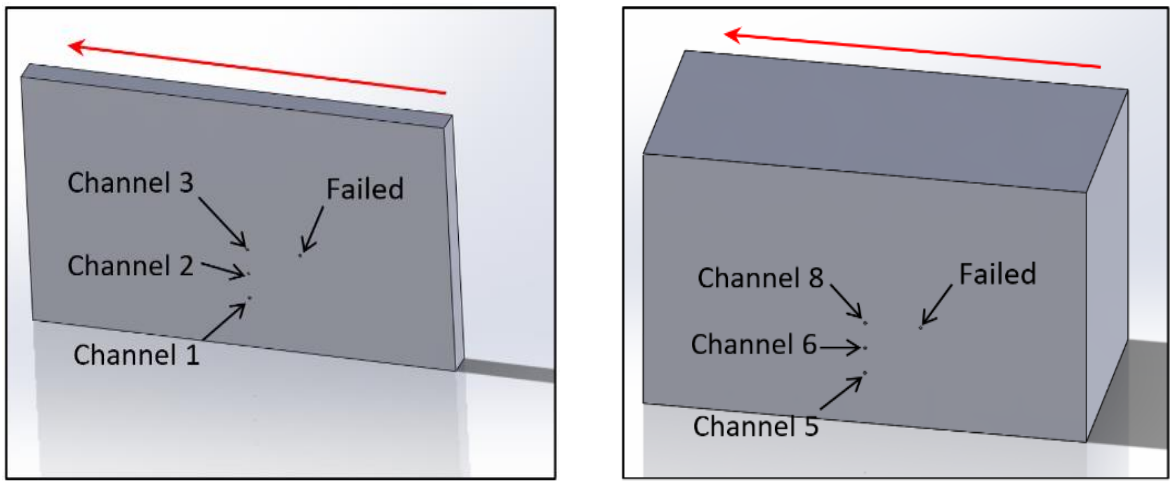

a) Thermocouples at thin wall b) Thermocouples at thick wall

FIGURE 5 – LOCATION OF THERMOCOUPLE CHANNELS IN THE POWDER-BED EXPERIMENT

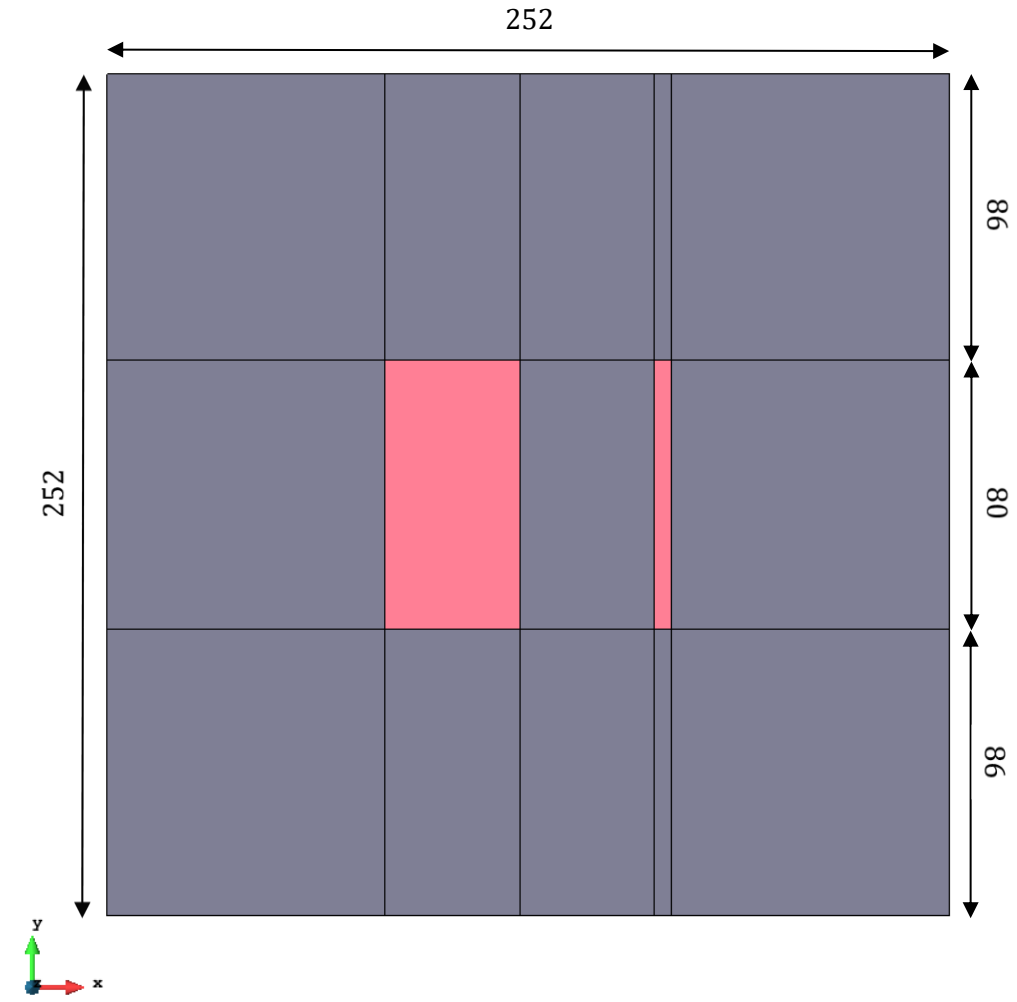

a) Plane XY view, units in [mm]

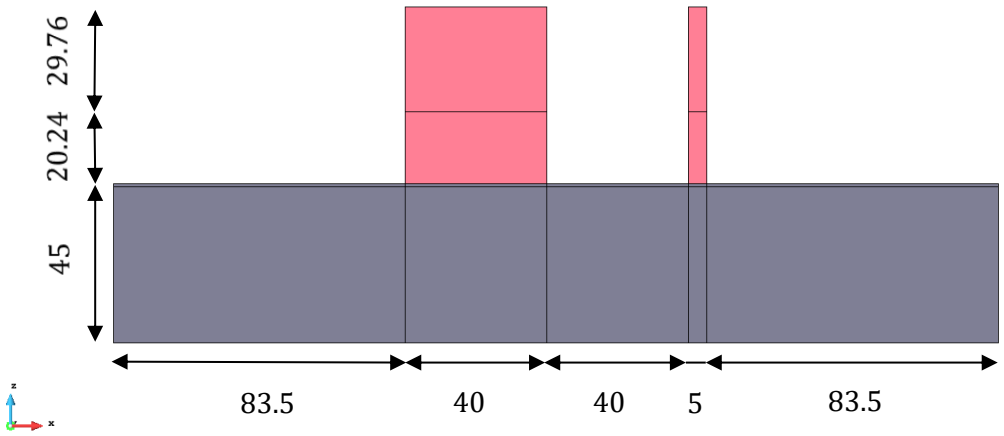

a) Plane XZ view, units in [mm]

FIGURE 6 – BASE PLATE AND WALLS IN THE POWDER-BED EXPERIMENT

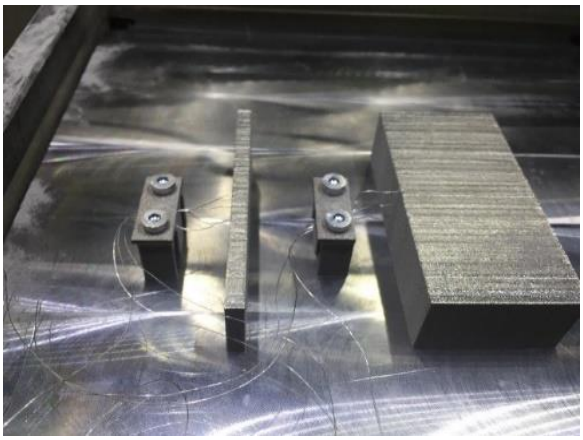

a) The printing job is interrupted at 20.24 [mm] height, the powder bed is removed, and 4 thermocouples are welded to each sample.

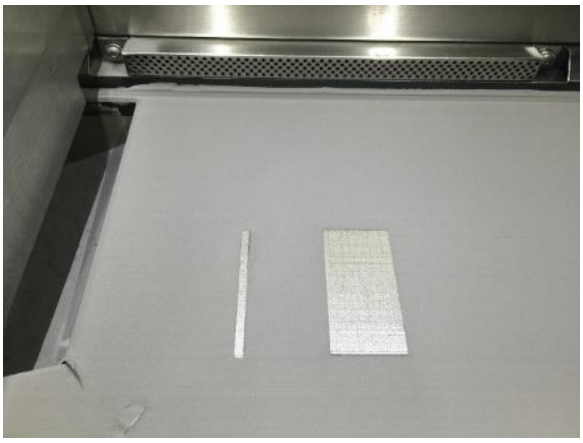

b) The powder bed is restored and the printing job was resumed.

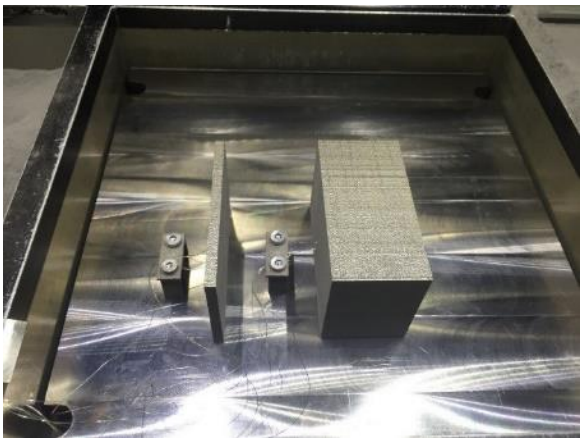

c) After finishing the printing job, the powder bed is removed from the building platform.

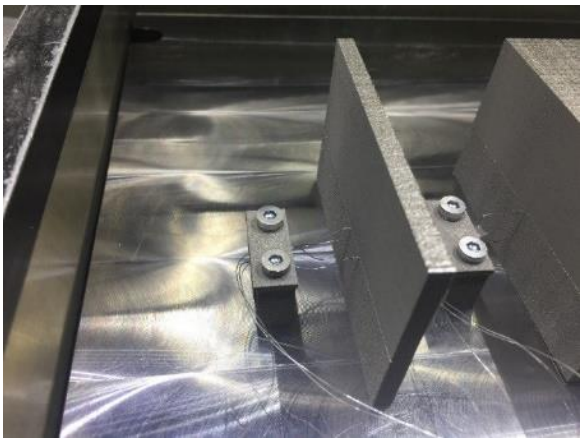

d) A closer picture shows the position of the thermocouples used throughout the printing process.

FIGURE 7 – STEPS TO CARRY OUT THE TEMPERATURE MEASUREMENTS

TABLE 2 shows the process parameters used for the printing process, being the default values suggested for the EOS-280 machine. A unidirectional scanning strategy is applied along the longitudinal direction of both samples. In FIGURE 8 the scanning sequence used for the printing process is described. The scanning path alternates between odd and even layers. Note that, the number of hatches drawn does not correspond to the actual number of hatches, which is notably higher according to the hatch distance value.

Power input	280	[W]
Scanning speed	1200	[mm/s]
Layer thickness	30	[µm]
Hatch distance	140	[µm]
Beam offset	15	[µm]

TABLE 2 - PROCESS PARAMETERS ADOPTED BY THE EOS MACHINE

Both the building platform and powder used to print the samples is Ti6Al4V Titanium alloy. The temperature-dependent properties of the bulk material [2], covering the range from room temperature to fusion temperature, are depicted in FIGURE 9. The solidification phase change is

characterized by a latent heat of L = 290 [kJ/kg], a liquidus temperature of 1703 [ºC], and a solidus temperature of 1697 [ºC].

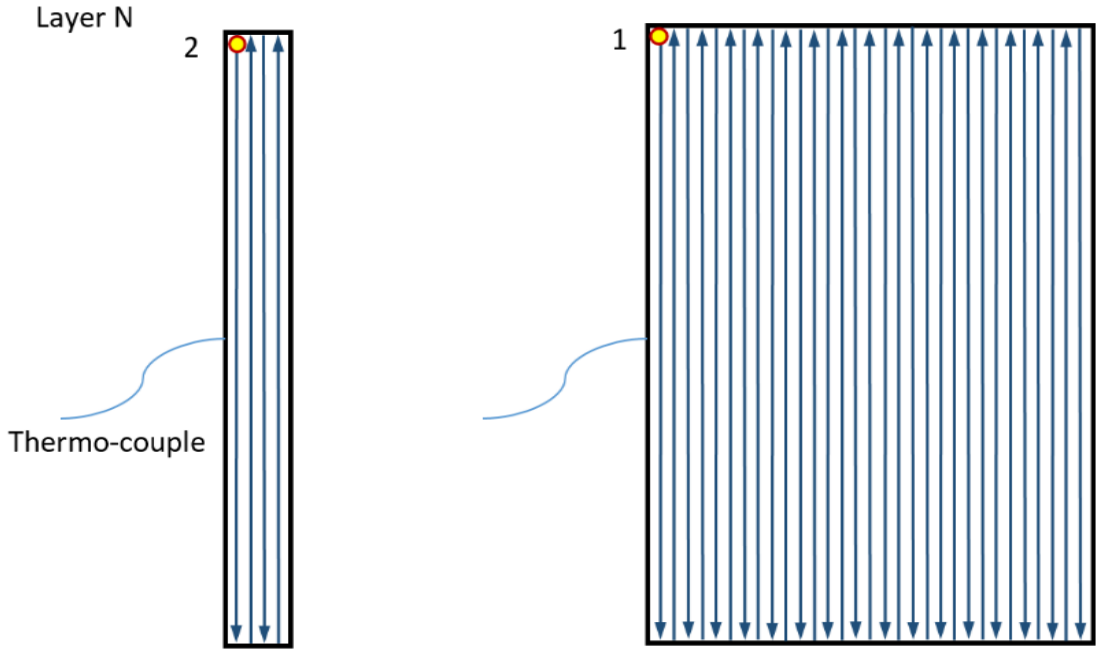

b) Pattern for odd layers. Starting points are indicated with circles.

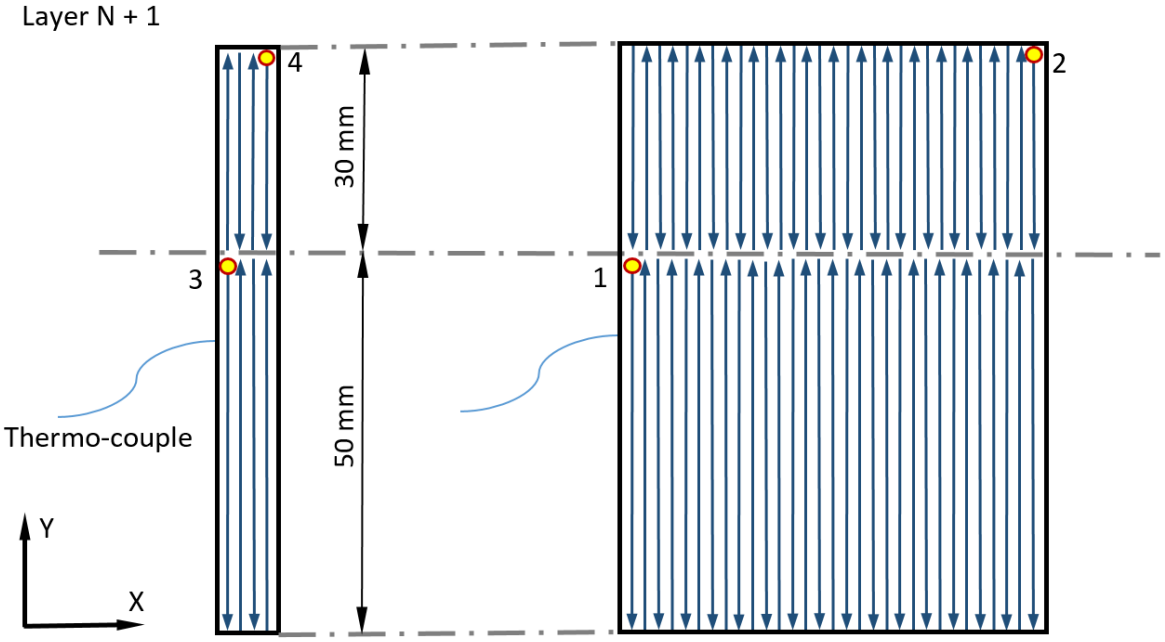

b) Pattern for even layers. Starting points are indicated with circles.

FIGURE 8 – SCANNING PATTERN IN THE POWDER-BED EXPERIMENT

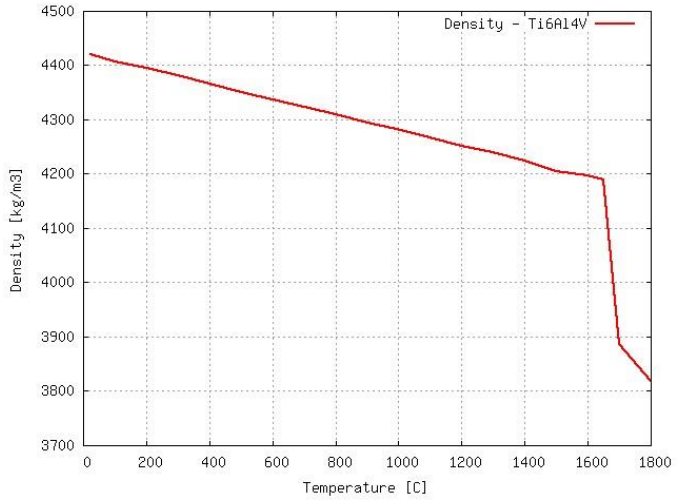

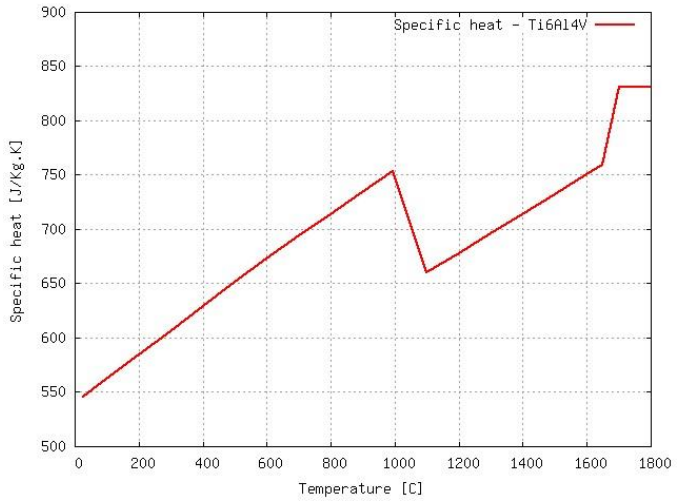

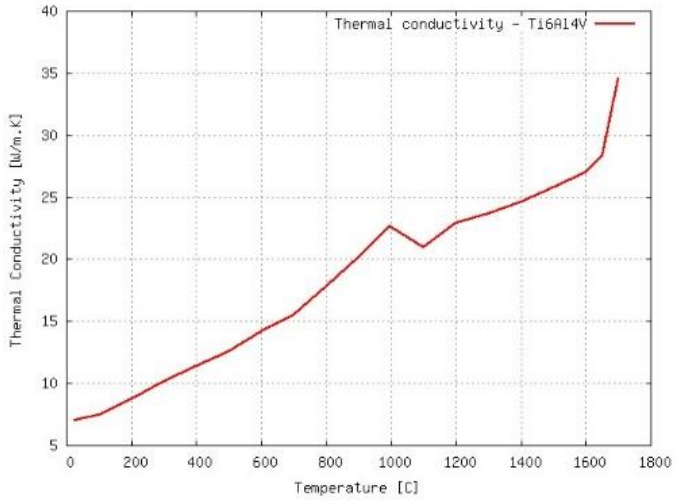

FIGURE 9 - TI6AL4V TITANIUM ALLOY
THERMAL BULK MATERIAL PROPERTIES [2]

Complimentary experiments were done to estimate the density of the powder when it is deposited layer-by-layer during the printing process. According to the measurements, the powder packing density is about 2405 [kg/m^3] at room temperature. Thus, the relative density of Ti64 powder is around 54% with respect to the density of the bulk material at room temperature.

2.2 NUMERICAL EXPERIMENTS AND RESULTS

The in-house research software COupled MEchanical and Thermal (COMET) was suitably enhanced to provide a finite-element framework for the heat transfer analysis of AM by powder-bed technologies. After the implementation tasks, the model was calibrated against the experimental data obtained at the MCAM research centre.

The FE discretization consists of a structured mesh of 76.224 hexahedral elements and 104.114 nodes. FIGURE 10 shows the numerical model considered for the numerical simulation of the printing process. This model does not only include the two walls but also the building platform because this is the responsible of heat dissipation by conduction. Its thermal inertia cannot be disregarded.

During the calibration process, the powder bed is excluded from the model, in order to reduce the computational cost. Hence, the heat loss by conduction through the powder bed was modelled through an equivalent heat flux.

To further decrease the computational cost of the model, the mesh size was adapted according to the different regions in the model. A smaller mesh size is defined for the thin wall, while a larger mesh is specified at the thick wall and the base plate.

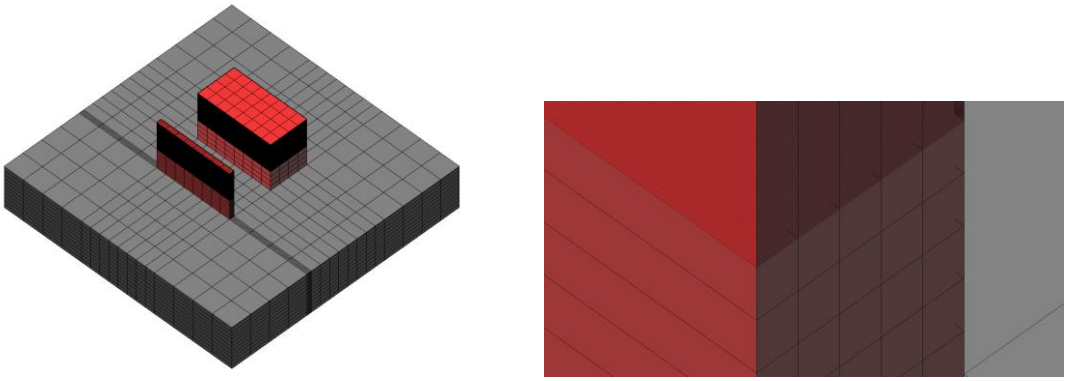

a) FE mesh b) The FE mesh conforms to the layers

FIGURE 10 – FE Mesh used for the numerical simulation with powder bed

The simulation starts when the printing job is resumed after placing the thermocouples and continues throughout the deposition of the remaining 992 layers, up to the cooling of the whole ensemble. Four different phases are considered when printing each new layer:

1. It is performed the scanning sequence corresponding to a new layer of the thin wall;
2. The laser moves from the thin wall to the thick wall (relocation time);
3. It is performed the scanning sequence corresponding to a new layer of the thick wall;
4. The platform is lowered and a new layer is spread. During this (recoat) time, the walls and the platform cool down.

The recoat and relocation times are shown in TABLE 3. Their values were estimated looking at the process videos.

Recoat time	9.36	[s]
Relocation time	0.03-0.06	[s]

TABLE 3 – RECOAT AND RELOCATION TIMES FOR THE AM PROCESS SIMULATION

The building platform is kept at 100ºC during the whole printing process. The average temperature of the powder as well as the temperature inside the chamber, used for the calibration of the heat transfer process (heat loss by convection and radiation), are set to constant values of 83ºC and 35 ºC, respectively.

The Heat Transfer Coefficient (HTC) for the heat convection model is set to 0.1 [W/m²K]. The heat loss by conduction through the powder is replaced by an equivalent HTC through the porous media, h_{powder} obtained as:

$$h_{\text{powder}} = \frac{k_{\text{powder}}}{t_{\text{powder}}} \tag{4.1}$$

where t_{powder} accounts for the average size of the powder bed. The value of the thermal conductivity, k_{powder} of metal powders is usually not provided by the vendor of the 3D printed machine and it is also not commonly catalogued. For this reason, it is frequently estimated with empirical expressions in terms of the conductivity of the bulk material, k_{bulk}, the conductivity of the surrounding air or gas, k_{gas}, and the porosity of the powder bed, φ. Among several models proposed in the literature for the prediction of thermal conductivity of powders, the work of Yagi and Kunii [6] for porous beds of metals as well as the revised version of Xue and Barlow [5] focused to low porosity powders is stated as:

$$k_{\text{powder}} = (6.3 + 22\sqrt{0.06\,\mathrm{k}_{\text{bulk}} - 0.016}\,)\frac{k_{\text{bulk}}(1-\varphi)}{\frac{\mathrm{k}_{\text{bulk}}}{\mathrm{k}_{\text{gas}}}(10^{0.523-0.594\varphi)}) - 1} \tag{4.2}$$

According to Equation (4.2), metal powders are expected to have a very low thermal conductivity. For instance, taking k_{Ti64} = 7 [W/mK] and $\mathrm{k}_{\text{argon}}$ = 0.016 [W/mK] at 20ºC, then the thermal conductivity is about 0.14 [W/mK]. Repeating the evaluation at 800ºC is 0.60 [W/mK]. This is in accordance with few available physical experiments. Hence, the average value of the powder conductivity used is $k_{\text{powder}} = 0.20$ [W/mK] while the average value of the size of the powder bed is: $t_{\text{powder}} = 80\,[mm]$, leading to an equivalent HTC through the porous media of $h_{\text{powder}} = 2.5\,\left[\frac{\mathrm{W}}{m^2\mathrm{K}}\right]$.

FIGURE 11 a) and b) describe the experimental data gathered at the six working thermocouples of both walls. Even if both samples are built using the same power density for the sintering process, they have very different thermal modulus, that is, ratio between their volume and the size of the external surfaces to dissipate the heat. Hence, it can be observed how the thick wall presents higher temperatures because of the higher thermal inertia compared to the thinner wall. To be commented that the temperature measurements coming from thermocouples CH3 and CH8 present extremely high oscillations at the beginning of the simulation because of the heat radiation process during the deposition of the first layers after resuming the printing process. Even if the thermocouples are protected against heat radiation, they will not provide reliable results unless they are far enough of the laser. For this reason, only the data from thermocouples CH1 and CH2 (for thinner sample) and thermocouples CH5 and CH6 (thicker sample) are taken into consideration in the calibration process.

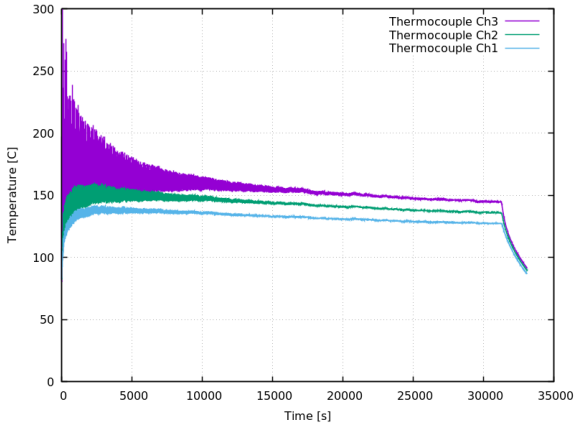

a) Measured data at thin wall

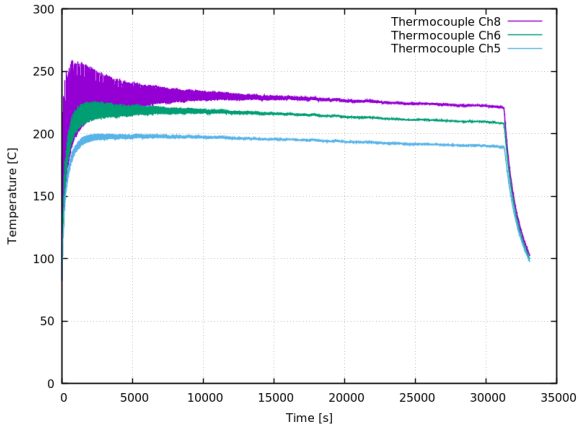

b) Measured data at thick wall

FIGURE 11 – Experimental data gathered for both sample locations

The model calibration has been performed using a **hatch-by-hatch** simulation strategy. This means that:

1. One single hatch is used to generate a new slice of the first sample (thin wall). The total amount of energy input used for the material sintering of the thin wall is spread at once.
2. In the following step, the laser is moved to the starting point of the thick wall ready for the sintering process.
3. Next, the sintering of the layer corresponding to the thick wall is performed in eight hatches.
4. A further time-step is performed to account for the recoating and relocation times when a new layer of powder is spread.

   Steps 1 to 4 are repeated until completing of the building process. Finally, the cooling process to the room temperature is analysed.

The hatching pattern of this simulation strategy is described in FIGURE 12. The process parameters used for the numerical simulation are gathered in TABLE 4. The scanning speed (printing) and the back speed (relocation, recoat) were scaled such that, for one layer, the sintering time and the relocation and recoat time were the same as the ones observed in the process videos.

Power input	280	[W]
Power absorption	45	[%]
Scanning speed	2.10	[mm/s]
Back speed	12.40	[mm/s]
Layer thickness	0.03	[mm]
Hatch width	5	[mm]

TABLE 4 - PROCESS PARAMETERS USED FOR THE HATCH-BY-HATCH STRATEGY

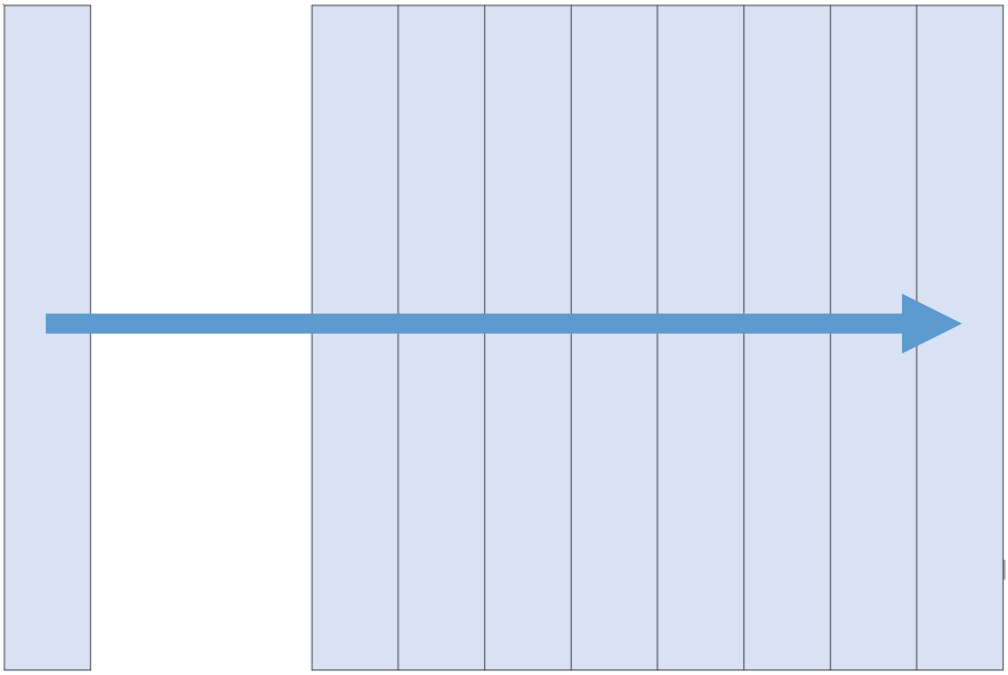

FIGURE 12 – HATCHING PATTERN AND SCANNING DIRECTION IN THE HATCH-BY-HATCH STRATEGY. THE HATCH WIDTH IS 5 [MM]

Thermocouples CH1 and CH2 have been used as target to get the most suitable simulation parameters to catch the experimental evidence and in particular to calibrate either the power absorption coefficient (responsible of the power input into the system) or the equivalent HTC between the sample and the powder bed (controlling the heat loss through the external surfaces of the samples). FIGURE 13 a) and FIGURE 13 b) compare the numerical results with the experimental measurements at CH1 and CH2. A very good agreement can be observed in the thermal response. The only mismatch can be observed during the final cooling process to reach the room temperature.

A lower accuracy of the numerical model can be observed in FIGURE 14 a) and b) when comparing the results obtained for the thick wall. This can be attributed to the approximation of the heat loss model. In particular, the powder temperature used cannot be considered as uniform for all the surfaces of the model. It is evident that the temperature of the powder in between the 2 samples should be higher than the average value used for the entire model. Nevertheless, the mismatch observed is less than 10%.

Remark 1: In the first stage of the experiment, the powder and the chamber gas are at room temperature, whereas the heat affected zone is at a much higher temperature. This heterogeneous temperature distribution is responsible for the highly oscillatory behaviour observed in the thermal response. As the build job advances, the temperature distribution becomes more homogeneous and the oscillations become smaller. However, the oscillations that take place at the beginning of the simulation cannot be well represented in the whole time frame plots, as in FIGURE 13 a) and FIGURE 14 a) (also in FIGURE 15 a) and FIGURE 17 a)). To see the actual trend of the experimental and numerical data at the first time steps of the simulation, these figures are accompanied with their corresponding close-up plots (b)).

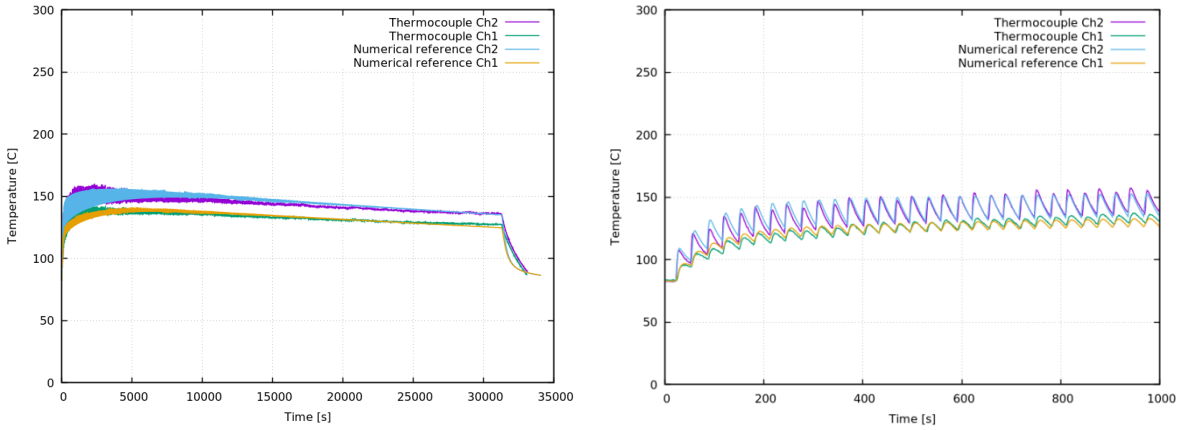

a) The entire sintering process

b) The first phase after resuming the build job

FIGURE 13 – NUMERICAL RESULTS AT THE THIN WALL FOR THE HATCH-BY-HATCH STRATEGY

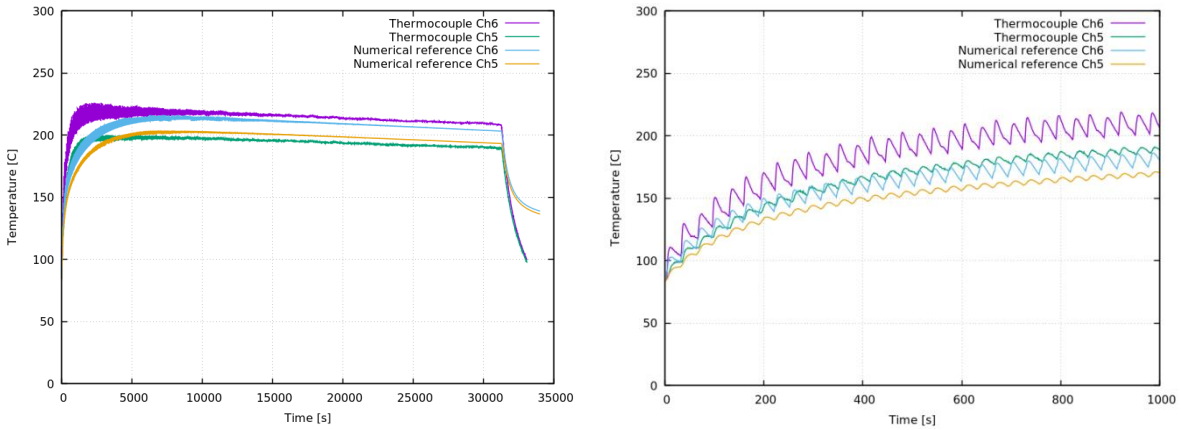

a) The entire sintering process

b) The first phase after resuming the build job

FIGURE 14 – NUMERICAL RESULTS AT THE THICK WALL FOR THE HATCH-BY-HATCH STRATEGY

As explained before, the numerical model takes as reference the physical response of the thin wall. This guided the calibration of the temperature of the powder, not known from the experimental campaign. A constant temperature of the powder of 83ºC yields good numerical results at the thin wall, but the value should be higher at the thick wall, to account for the higher energy that it is being applied. In fact, the temperature of the powder in the model should vary in time, but this increases the difficulty of the calibration tasks.

Additional numerical experiments were carried out modifying the simulation strategy.

Different analyses were made trying to include the powder-bed into the model. In this case, the size of the FE discretization is much bigger including 594.368 hexahedral elements and 649.230 nodes. This model is about six times bigger than the previous one without including the powder-bed. The computational time required is almost 4 times longer (from 6h to about 1 day). This increase in computational cost explains why this model has not been selected to carry out the calibration sequence.

FIGURE 15 a) and b) compare the numerical result with and without including the powder bed in the simulation.

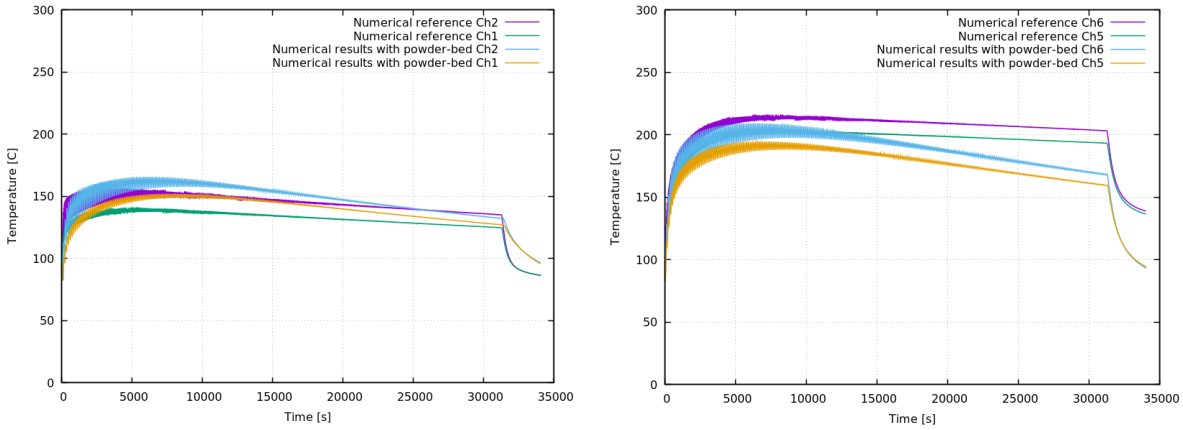

a) At the thin wall b) At the thick wall

FIGURE 15 – NUMERICAL RESULTS WITH AND WITHOUT INCLUDING THE POWDER-BED INTO THE MODEL

A constant value for the thermal conductivity of the powder: k_{powder} = 0.20 [W/mK] is assumed. The results are not as good as in the previous case. This is due to different reasons. Even if the model is more realistic because it includes the powder, the results depend on more material parameters which require a more complex calibration analysis. In fact, the powder must be characterized by all the corresponding thermo-physical properties: density, specific heat and conductivity, all of them as a function of the actual temperature field. The available limited characterization of the powder bed makes difficult the thermal analysis of the manufacturing process including it into the model. Furthermore, the high computational cost makes also extremely slow the sensitivity analysis to calibrate the model when considering the powder bed.

A different strategy has been employed trying to reduce as much as possible the simulation time while keeping reasonable result accuracy. The idea consists of a **layer-by-layer** building strategy. This means that:

1. One single step is used to simulate a new slice for both samples. Hence, during this period the sintering of the 2 sections of the model is performed simultaneously. The energy density used during the whole scanning sequence is spread homogeneously at once. The sintering time includes the relocation time, that is, the time used by the laser to move from the ending point of scanning sequence of thin wall to the starting point of the thick wall.
2. The following time-step is performed to account for the recoating and relocation times when a new layer of powder is spread.

Steps 1 and 2 are repeated until completing of the building process. Finally, the cooling process to the room temperature is analysed.

The scanning pattern of this simulation strategy is described in FIGURE 16. The process parameters used for the numerical simulation are gathered in TABLE 4, including the new scaling of the scanning speed and the back speed for this new scanning strategy.

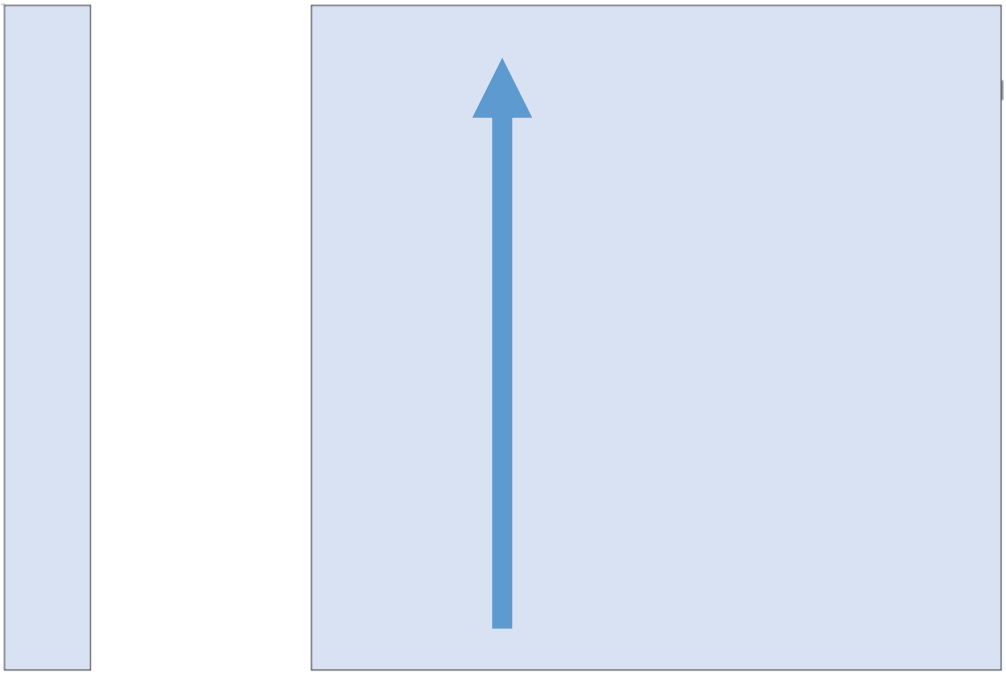

FIGURE 16 – SCANNING PATTERN IN THE LAYER-BY-LAYER STRATEGY. THE SCANNING DIRECTION IS VERTICAL.

Power input	280	[W]
Power absorption	45	[%]
Scanning speed	3.73	[mm/s]
Back speed	0.69	[mm/s]
Layer thickness	0.03	[mm]
Hatch width	5	[mm]

TABLE 5 - PROCESS PARAMETERS USED FOR THE LAYER-BY-LAYER STRATEGY

Similarly, an n-layer-by-n-layer simulation strategy can be defined, because it allows for reducing significantly the computational cost (almost n-time). In FIGURE 17, both layer-by-layer and 4-layer-by-4-layer strategies are shown and their results compared to the hatch-by-hatch strategy used as a reference. Observe that, when using a layer-by-layer strategy an average heat input is used and the corresponding energy density is spread simultaneously. Hence, the temperature plots must be intended as an approximate evolution of the temperature field of the layer without a direct relationship with the measurement points. Clearly, the advantage is in the CPU-time which is notably reduced as shown in TABLE 6.

Strategy	CPU-time [h]	[%]
Reference	6	100
Hatch-by-hatch with powder	24	400
Layer-by-layer	1	17
4-layer-by-4-layer	0.33	6
High-fidelity	32	533

TABLE 6 – SIMULATION CPU-TIME USING DIFFERENT STRATEGIES

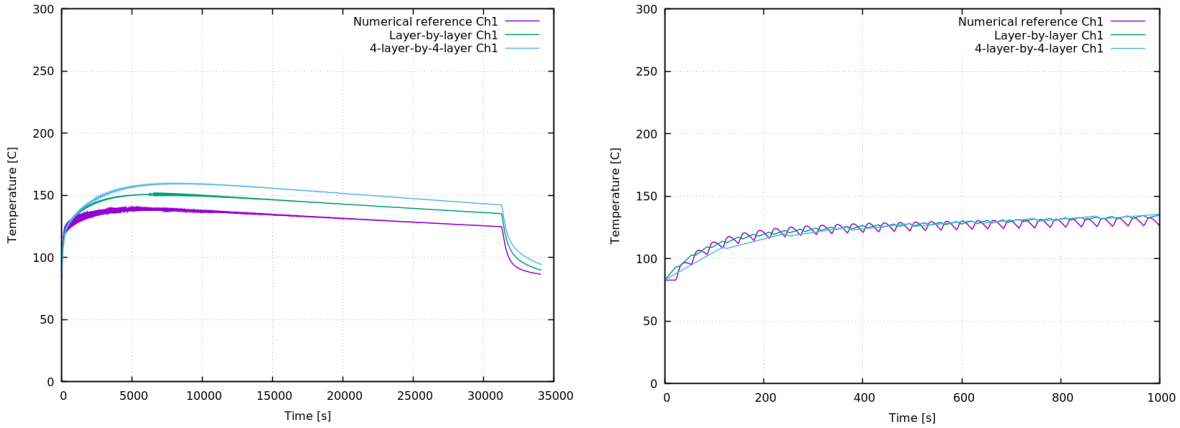

a) The entire sintering process

b) The first phase after resuming the build job

FIGURE 17 – NUMERICAL RESULTS WITH A LAYER-BY-LAYER AND A 4-LAYER-BY-4-LAYER SIMULATION

Finally, the focus of the simulation strategy has been to look for the highest accuracy. This means that, careless the computational cost, the scanning sequence has been defined to be as close as possible to the local hatching strategy as operated by the EOS machine. This simulation strategy is referred to as high-fidelity. The scanning pattern is described in FIGURE 18 and the process parameters are detailed in TABLE 7. In this case, the hatch width has a value of 1 [mm]. FIGURE 19 compares the temperature evolution at the thermocouple locations CH1 and CH2 comparing with the hatch-by-hatch strategy and the experimental data. The good correlation between the two proposed strategies makes use of the high-fidelity strategy less interesting, since the required computational time is 5 times longer (from 6h to about 32h).

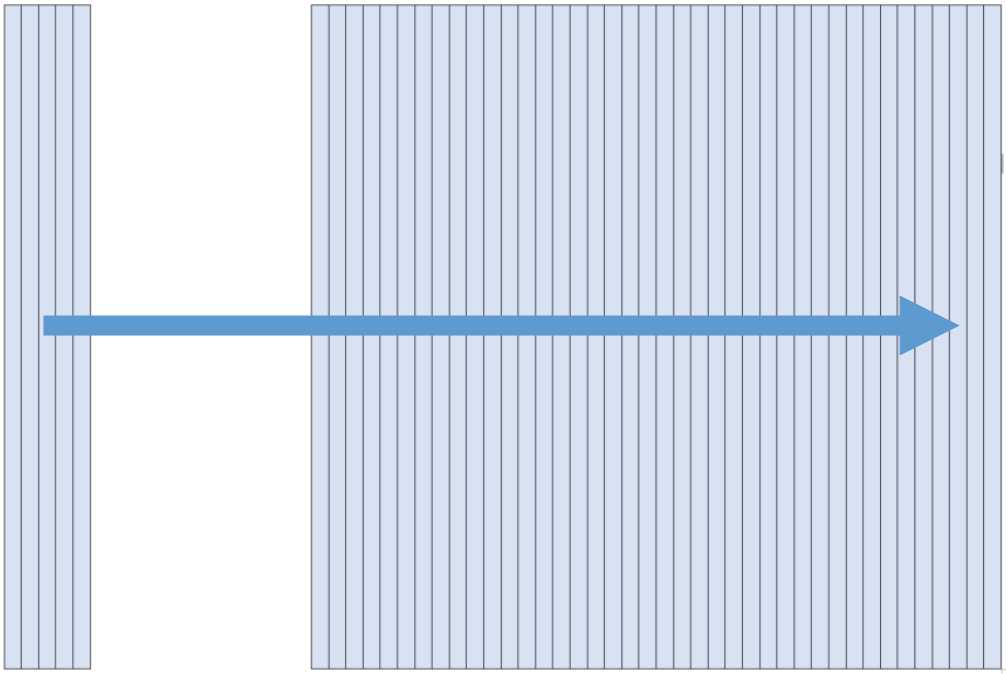

FIGURE 18 – HATCHING PATTERN AND SCANNING DIRECTION
IN THE HIGH-FIDELITY STRATEFGY. THE HATCH WIDTH IS 1 [MM]

Power input	280	[W]
Power absorption	45	[%]
Scanning speed	2.10	[mm/s]
Back speed	12.40	[mm/s]
Layer thickness	0.03	[mm]
Hatch width	5	[mm]

TABLE 7 - PROCESS PARAMETERS USED FOR THE HIGH-FIDELITY STRATEGY

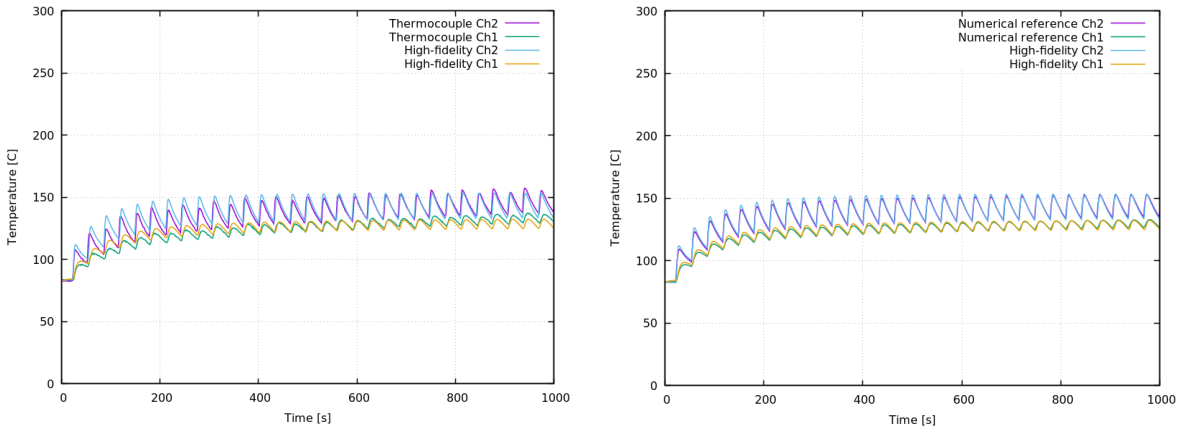

a) Comparison with experimental data b) Comparison with numerical reference

FIGURE 19 – NUMERICAL RESULTS WITH A HIGH-FIDELITY SIMULATION

3 MODEL CALIBRATION FOR BLOWN-POWDER METHODS

3.1 EXPERIMENTAL SETTING

An experimental campaign took place at the *State Key Laboratory of Solidification Processing* (SKLSP) in Xi'an, China, to calibrate and validate the numerical model described in *Deliverable 4.2 Thermal analysis framework for MD process* for the simulation of AM processes with blown-powder technologies [2].

The experimental tests were carried out using the laser solid forming (LSF-III) machine in FIGURE 20a). The printing system employs a CO_2-laser with a maximum power input of 4 [kW] in a closed chamber with a protection atmosphere (argon). A numerical control device controls the movement of the powder-feeding coaxial nozzle, represented in FIGURE 20b).

c) LSF Machine at SKLSP

d) Powder-feeding nozzle

FIGURE 20 - EXPERIMENTAL FACILITES AT SKLSP

The substrate samples are 140x50x6 [mm] Titanium alloy plates that have been previously burnished by sand paper and cleaned using anhydrous-alcohol and acetone. Five OMEGA GG-K-30 thermocouples connected to a midi LOGGER G900-4/8 are spot-welded: three on the lower surface and two more on the upper surface, as shown in FIGURE 21 and FIGURE 22.

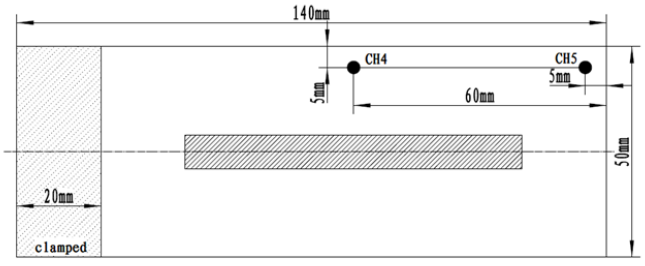

FIGURE 21 - THERMOCOUPLES AT UPPER SURFACE

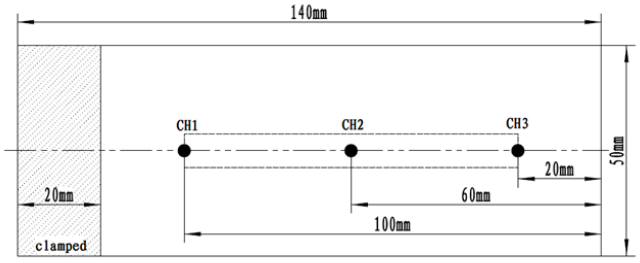

FIGURE 22 - THERMOCOUPLES AT LOWER SURFACE

The substrate is clamped to a supporting structure made of stainless steel, as represented in FIGURE 24a). This clamping system has not been included in the numerical model, even though its thermal inertia has a clear impact on the temperature evolution at the contact interface with the substrate.

The process parameters that were input to the control system of the LSF machine are gathered in TABLE 8. The up-lift of the nozzle is 0.3 [mm], assuming this is the incremental height of each deposited layer. Two velocities are associated to the movement of the laser-head: the scanning-speed when the laser is switched-on, and the back-speed when the laser is switched-off and it is repositioning.

Power input	2	[kW]
Laser beam size	1.6	[mm]
Offset distance	0.8	[mm]
Up-lift height	0.3	[mm]
Scanning speed	10	[mm/s]
Back speed	50	[mm/s]
Powder feeding	8.5	[r/min]

TABLE 8 - PROCESS PARAMETERS INFORMED TO THE LSF MACHINE

The scanning path is described in FIGURE 23. This sequence is repeated 10 times to build 10 layers of added material, up to a metal deposition of approximately 3 [mm] high. At the end of the process, as seen in FIGURE 24b), the planned dimensions of the printed body are 80x6.4x3 [mm].

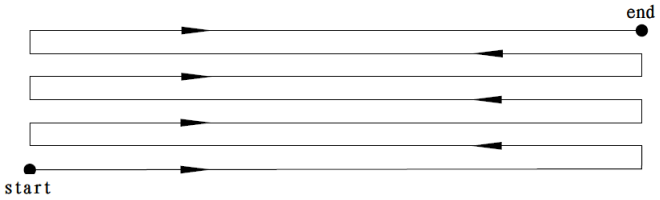

FIGURE 23 - SCANNING SEQUENCE OF A LAYER

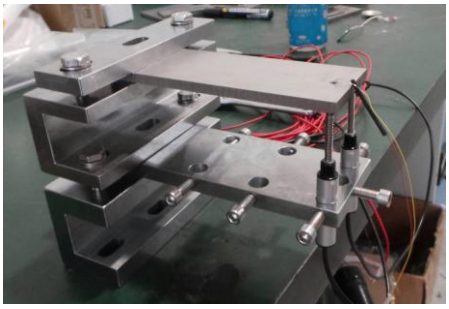

a) Substrate and supporting system

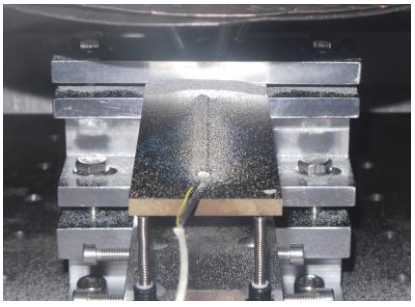

b) Powder-feeding nozzle

FIGURE 24 – SUBSTRATE PLATE AND SUPPORTING SYSTEM IN THE EXPERIMENTAL CAMPAIGN

Finally, both the substrate and the powder fed in the AM process are also made of (Ti6Al4V) Titanium alloy, as in the previous experiment of Section 2. The temperature-dependent material properties of this alloy are described in FIGURE 9.

3.2 NUMERICAL EXPERIMENTS AND RESULTS

A finite-element model for the heat transfer analysis of AM by blown-powder method was implemented in the in-house research code COMET. This section describes the calibration of this model against the measurements obtained from the physical experiments at the SKLSP research facilities, described in Section 3.1. The numerical results are presented in terms of temperature plots at the different thermocouple locations on the substrate.

Three distinct phases are considered in the simulation: first, the pre-heating phase, then, the manufacturing phase, and, finally, the cooling phase. During the pre-heating phase the efficiency of the laser is lower, because the temperature of the substrate is not high enough. As a result of this, less powder is sintered and the printed body has an actual size of 80x7x2.8 [mm].

Even though the planned and actual dimensions of the metal deposition differ by less than 10%, the actual dimensions have been taken as reference for the FE discretization, in order to avoid over-estimating the thermal inertia of the sintered material.

According to this, the FE mesh used for the calibration consists of 12.456 nodes and 10.050 linear hexahedral elements, as seen in FIGURE 25. A finer structured mesh of 2.5x0.875x0.28 [mm] elements is used at the process zone to properly capture the high temperature gradient induced by the energy input and to adapt to the scanning pattern and process parameters, whereas the size of the elements is bigger at the substrate of the plate.

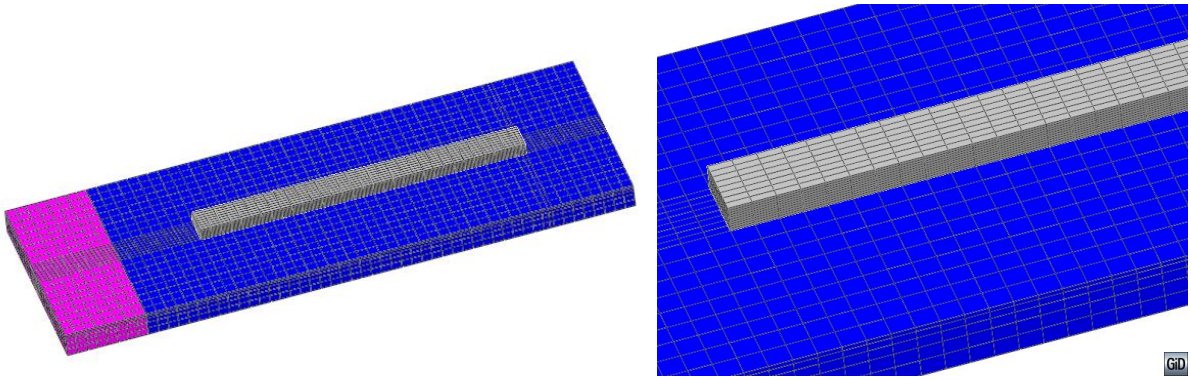

a) FE mesh

b) Detail of the FE mesh at the process zone

FIGURE 25 – FE MESH USED FOR THE NUMERICAL SIMULATION WITH BLOWN POWDER

Furthermore, the process parameters have been updated to take into account the actual metal deposition dimensions. In this case, the layer thickness is set to 0.28 [mm], while the laser beam size is set to 1.75 [mm], with 50% overlapping during the scanning operation.

Most of the energy input is scattered in the surrounding environment. This is accounted for in the power absorption coefficient, a measure of the efficiency of the laser. The power absorption coefficient is the most sensitive parameter of the numerical model [2].

In powder-bed technologies, the laser is focussed on the powder that has been spread to build up the new layer. However, in blown-powder technologies, the laser is focussed on the substrate or the previously deposited layer. From the numerical point of view, this is taken into account by assigning the heat source term to the elements just below the elements to be activated in the new layer.

Power input	2	[kW]
Power absorption	16.5	[%]
Laser beam size	1.75	[mm]
Overlapping	50	[%]
Scanning speed	10	[mm/s]
Back speed	50	[mm/s]
Penetration	0.28	[mm]
Layer thickness	0.28	[mm]

TABLE 9 - PROCESS PARAMETERS USED FOR THE NUMERICAL SIMULATION

The pink region in FIGURE 25 represents the surface in contact with the clamping system that restrains the movement of the substrate plate. At this contact interface the heat loss is by heat conduction between the plate and the clamping system. The heat transfer coefficient used for Newton's law of cooling is 50 [W/m^{2}K].

The temperature of the supporting structure is usually assumed constant throughout the analysis because its thermal inertia is much higher than the one of the sample. However, according to the measurements given in FIGURE 26, this was not the case in this experimental setting. For this reason, the evolution in time of the contact temperature with the clamping system was included in the numerical model, also described in FIGURE 26.

At the surfaces of the blue and grey regions of FIGURE 25 heat is dissipated through the surrounding environment. The manufacturing process is carried out in a closed chamber with a protection atmosphere to prevent oxidation. In this case, the environment temperature was also not constant. FIGURE 26 b) shows the environment temperature measured with a thermocouple. The oscillations are due to a measurement location placed too close to the process area. Hence, they were affected by the heat radiation induced by the AM process. The HTC coefficient used for the heat convection model is 10 [W/m^{2}K], while the emissivity coefficient used for the heat radiation model is 0.7.

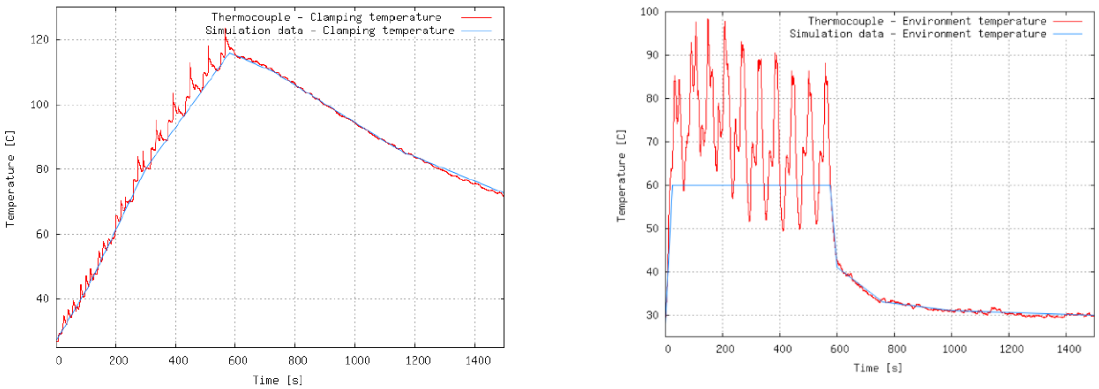

a) Temperature at the clamping system b) Environment temperature

FIGURE 26 – TEMPERATURE AT THE CONTACT WITH THE CLAMPING SYSTEM AND AT THE SURROUNDING ENVIRONMENT: MEASURED DATA AND APPROXIMATE LAWS USED IN THE NUMERICAL SIMULATION

FIGURE 27 shows both measured and calculated temperatures at the lower and upper surfaces, respectively. The agreement is remarkable. A closer view is presented in FIGURE 28, where it is possible to appreciate the accuracy of the numerical results.

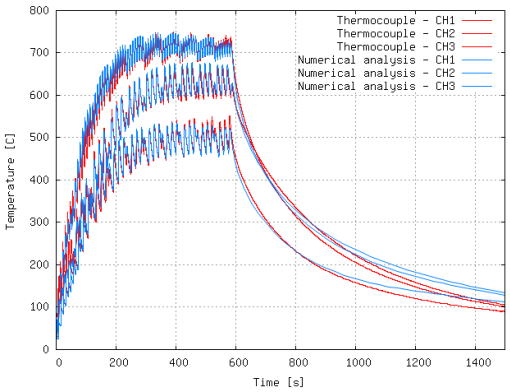

c) Lower surface thermocouples

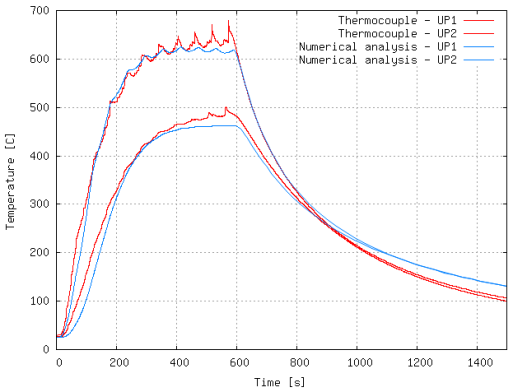

d) Upper surface thermocouples

FIGURE 27 – TEMPERATURE EVOLUTION AT THE 5 APPOINTED THERMOCOUPLE LOCATIONS. COMPARISON BETWEEN EXPERIMENTAL EVIDENCE AND THE NUMERICAL RESPONSE.

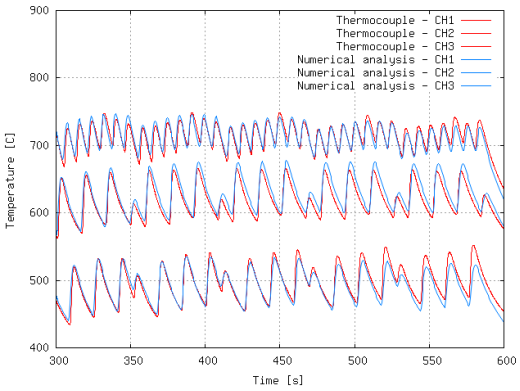

a) Lower surface thermocouples

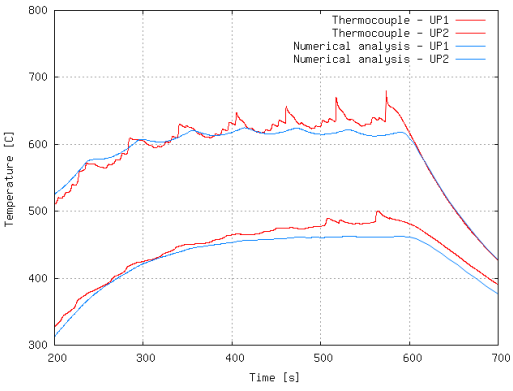

b) Upper surface thermocouples

FIGURE 28 – DETAIL OF TEMPERATURE EVOLUTION AT THE 5 APPOINTED THERMOCOUPLE LOCATIONS

FIGURE 29a) shows the sample after cooling at room temperature with the mark induced by the red-hot temperature field. FIGURE 29b) shows the temperature contour-fill at the end of the AM process just before cooling. Once again there is a good agreement between the two sets of data.

Remark 2: Thermocouples 4 and 5 are placed on the upper surface of the substrate and were shielded against heat radiation. In spite of this, the recorded temperatures are still perturbed by heat radiation effects.

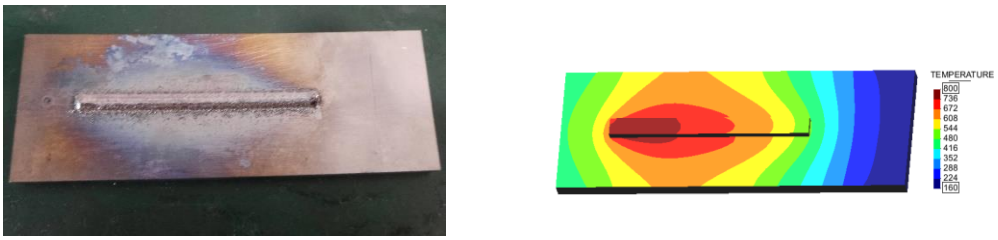

a) Oxidation after AM process b) Temperature contour-fill at the end of the AM process

FIGURE 29 – TEMPERATURE CONTOUR-FILL AT THE END OF THE MANUFACTURING PROCESS. COMPARISON WITH THE RESIDUAL SAMPLE MARK.

Finally, FIGURE 30 describes the numerical response considering a *layer-by-layer* activation sequence. In this situation, the balance of energy allows for an average estimation of the temperature profiles, but all the details in the temperature history produced by the scanning sequence are lost.

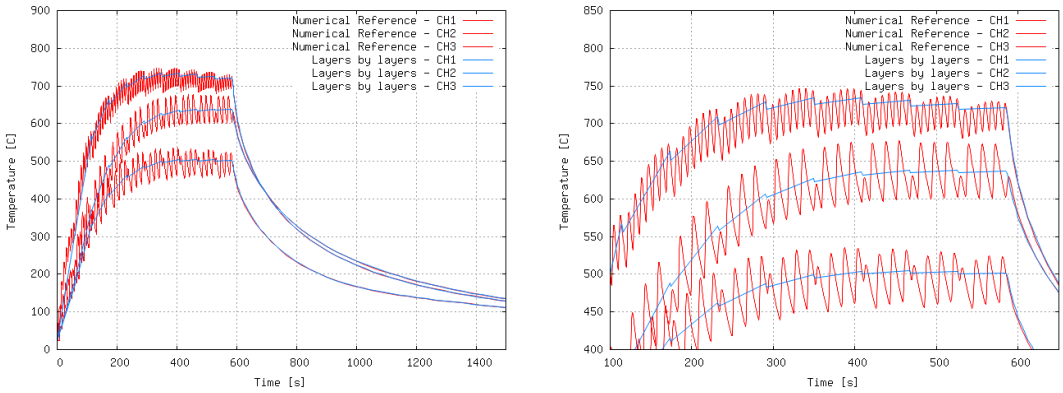

a) Temperature at lower thermocouples b) Detail of temperature evolution

FIGURE 30 – METAL DEPOSITION BY BLOWN POWDER CONSIDERING A LAYER-BY-LAYER SCANNING SEQUENCE

4 CONCLUSIONS AND FUTURE WORK

The numerical framework developed for the numerical simulation of the heat transfer analysis in Additive Manufacturing processes using metal powder technologies, both powder-bed and blown-powder has been experimentally calibrated.

From the simulation point of view, the main differences between the two AM technologies analysed concern the heat dissipation mechanisms: heat conduction through the powder bed and the base plate in powder-bed methods, heat convection and radiation through the external surface in blown-powder methods.

The experimental calibration of the model used for the numerical simulation of the powder-bed technology has been performed in collaboration with the *Monash Centre for Additive Manufacturing* (MCAM) in Melbourne, Australia. The main challenge during calibration was to find the appropriate estimations for the heat transfer coefficients between the component and the powder bed. In spite of this, a reasonably good agreement between the numerical response and the experimental data has been achieved.

Even though the target technology in the CAxMan project is the powder-bed technology, and more specifically, the Direct Metal Laser Sintering with the EOS M280 machine, the numerical model has also been successfully calibrated for blown-powder technology. This calibration work hasbeen carried out at the *State Key Laboratory of Solidification Processing* (SKLSP) in Xi'an, China.

REFERENCES

[1] A. Bachorski, M. Painter, A. Smailes, and M. A. Wahab. Finite-element prediction of distortion during gas metal arc welding using the shrinkage volume approach. *Journal of Materials Processing Technol ogy*, 92:405–409, 1999.

[2] M. Chiumenti, X. Lin, M. Cervera, W. Lei, Y. Zheng, and W. Huang. Numerical simulation and experimental calibration of additive manufacturing by blown powder technology. part i: thermal analysis, Rapid Prototyping Journal, in press, 2016.

[3] Holman, J.P., Heat Transfer, 7th ed., McGraw Hill Book Company, New York, 1990.

[4] Schlichting, H. "Boundary-layer theory, 6th edn. Translation by Kestin J. Chaps 14 and 20." (1979).

[5] Xue, S., & Barlow, J. W. Models for the Prediction of the Thermal Conductivities of Powders. In Solid Freeform Fabrication Symposium Proceedings (pp. 62-69). Austin, Tex.: Center for Materials Science, University of Texas at Austin, 1991.

[6] Yagi, S., & Kunii, D. Studies on effective thermal conductivities in packed beds. AIChE Journal, 3(3), 373-381, 1957.